DE GRUYTER
Open Physics 2025; 23: 20250188

Research Article

Humaira Yasmin*, Rawan Bossly, Fuad S. Alduais, Afrah Al-Bossly, and Anwar Saeed

Numerical solution and stability analysis of non-Newtonian hybrid nanofluid flow subject to exponential heat source/sink over a Riga sheet

https://doi.org/10.1515/phys-2025-0188
received November 20, 2024; accepted June 24, 2025

Abstract: The non-Newtonian (NN) hybrid nanofluids (HNF) flow over a porous stretching or shrinking Riga sheet is calculated. The HNF is produced by the scattering of cerium oxide (CeO_2) and aluminum oxide (Al_2O_3) nanoparticles. NN HNF offers a wide variety of uses. For instance, enhanced heat transportation, cooling, maintenance, and reliability in mechanically powered delivery of medicines, increased efficacy in microfluidic devices, advanced material synthesis, and energy-related applications such as storing energy and solar power generation systems are a few of them. For this purpose, the flow phenomena are modeled in the form of nonlinear partial differential equations (PDEs), which are reduced into the dimension-free form through the similarity conversion. The solution is obtained by using the numerical approach parametric continuation method. The stability analysis has also been performed to check which solution is stable and reliable in practice. The results are compared to the numerical outcomes of the published studies. The present findings have shown the best correlation with the previous published studies. The relative error between the published and present study at Pr = 10 (Prandtl number) is 0.00046%, which is gradually reduced up to 0.00202% with the variation of Pr = 0.7. Furthermore, the impact of a viscoelastic factor enhances the velocity field of HNF (Al_2O_3 and CeO_2/SA) for both types of NN fluids (second-grade fluid & Walter's B fluid) in the case of stretching Riga sheet.

Keywords: Arrhenius activation energy, stability analysis, non-Newtonian fluid, hybrid nanofluid, numerical solution, Riga sheet

Nomenclature

AAE	Arrhenius activation energy
Al_2O_3	aluminum oxide
c	electrode width
C	concentration
CeO_2	cerium oxide
C_p	heat capacitance (J kg^{-1} K^{-1})
CRs	chemical reactions
Ea	activation energy
HNF	hybrid nanofluids
j_0	current density
K	surface permeability
k	thermal conductivity (kg ms^{-3} K^{-1})
k_r	rate of chemical reaction
M_0	magnetization of the Riga plate
NN	non-Newtonian
NPs	nanoparticles
Q_h	Hartmann number
q_r	heat radiation
SG	second-grade
SA	sodium alginate
RP	Riga plate
T	temperature
$u,\ v$	velocity component
V_T	thermophoretic velocity
WB	Walter's B
$\alpha_1 > 0$	SG fluid
$\alpha_1 < 0$	WB fluid
β_1	magnitude and width of electrodes
ρ	density (kg m^{-3})
ρC_p	thermal capacity

*** Corresponding author: Humaira Yasmin,** Department of Basic Sciences, General Administration of Preparatory Year, King Faisal University, P.O. Box 400, Al Ahsa, 31982, Saudi Arabia; Department of Mathematics and Statistics, College of Science, King Faisal University, P.O. Box 400, Al Ahsa, 31982, Saudi Arabia, e-mail: hhassain@kfu.edu.sa
Rawan Bossly: Department of Mathematics, College of Science, Jazan University, Jazan 82817, Saudi Arabia
Fuad S. Alduais, Afrah Al-Bossly: Department of Mathematics, College of Science and Humanities in Al-Kharj, Prince Sattam bin Abdulaziz University, Al-Kharj, 11942, Saudi Arabia
Anwar Saeed: Department of Mathematics, Abdul Wali Khan University, Mardan, Khyber Pakhtunkhwa, 23200, Pakistan

$\lambda < 0$	dwindling sheet
$\lambda > 0$	stretching sheet
σ	electrical conductivity

1 Introduction

The Riga plate (RP), a device or plate made up of a flat surface with specified electrodes and patterns, is commonly used in fluid dynamics to investigate the behavior of electrically conductive fluids including electrolytes and liquid metals. By supplying voltage, the Riga plate creates an electric field that generates electrohydrodynamic (EHD) flows, enabling researchers to alter fluid motion, improve mixing, and manage instabilities in a variety of applications. Stretching Riga plates, for example, can improve techniques for mass transfer and allow for accurate droplet manipulation in microfluidics, making them particularly useful in biomedical applications and chemical reactors. Furthermore, their use in cooling systems improves thermal management by facilitating effective heat transfer *via* fluid flow regulation [1–3]. Cui *et al.* [4] studied the nanofluid (NF) flow in a porous media over a Riga surface, with the impact of convective boundary conditions, and activation energy. It was discovered that the Hartman and Eckert numbers increase with both temperature and velocity profiles. Algehyne *et al.* [5] assessed the magnetohydrodynamics (MHD) hybrid nanofluids (HNF) flow consisting of MgO–Ag/water with motile microbes across a Riga sheet with the impact of slip conditions and activation energy. It was noticed that the velocity slip conditions drop the thermal curve and velocity rate of NF. Mohanty *et al.* [6] investigated the influence of interfacial nanolayer width on multi-walled carbon nanotubes and nano-diamond incorporated in water-based HNF fluid flow along an inclined stretching cylinder. Farooq *et al.* [7,8] studied the MHD NF flow consisting of SiO_2 and MoS_2 nanoparticles (NPs) with temperature-dependent viscosity across a stretching sheet. It was observed that increasing the magnetic factor lowers fluid velocity while increasing the temperature curve. Bilal *et al.* [9] numerically analyzed the mass distribution and energy transfer through NF flow over an expanding Riga plate. It was noticed that the fluid flow rate lowers with the impact of the power law index and improves with the outcome of the modified Hartmann number. Xin *et al.* [10] investigated how the discharge of pollutants concentration influences the non-Newtonian (NN)-NF flow across a permeable RP and discovered that the energy transmission rate of the second-grade (SG) fluid enhances up to 6.25%, while Walter's fluid B rises to 7.85%. Gangadhar *et al.* [11] calculated that the improved slip and convective heat conditions influence the ternary NF flow across a RP and concluded that the variation in Hartmann number drops the fluid velocity. Bilal *et al.* [12] numerically simulated the pollutant discharge concentration impact on NN HNF flow for the treatment of wastewater for industrial uses across a Riga surface.

NN fluids, which feature complex flow behavior that differs from Newton's viscosity law, are used in a variety of sectors. In medicine, they are utilized in the manufacture of pharmaceuticals and biological compounds, where their distinct features enhance the delivery of drugs and results for patients. NN fluids are essential in food processing for items such as sauces and dressings, where their viscosity can be adjusted for the best consistency and texture. Furthermore, in the construction sector, materials such as cement and various adhesives depend upon NN behavior to improve workability and efficiency. NN fluids are also used in the creation of body armor and smart fluids for automobiles, where their viscosity may alter under stress to provide better protection and functionality [13]. Mohanty *et al.* [14,15] investigated the irreversibility analysis of 3D Casson HNF flow induced by a turning disc employing a Runge–Kutta–Fehlberg-based shooting method. Farooq *et al.* [16] evaluated the stagnation point mixed convective ternary HNF flow over a vertical Riga sheet employing Al_2O_3, SiO_2, and TiO_2 NPs in the base fluid. When the mixed convection factor is employed, the thermal profile of HNF decreases, while the distribution of velocity improves. Cham and Mustafa [17] provided a thorough assessment of the effect of viscoelastic factor and partial slip conditions on the axial fluid flow caused by a plate or cylinder deforming with linear acceleration. Farooq *et al.* [18] addressed the thermal transportation of NN fluids containing carbon nanotubes NPs across a stretched surface, taking into account viscosity dissipation, porous medium, heat source, and magnetic field parameters. It was discovered that increasing the SG fluid factor increases the velocity dissemination, whereas increasing the magnetic and porosity parameters reduces the velocity dispersion. Ahmad *et al.* [19] discussed the importance of irreversible processes in the regular Homann flow of viscoelastic liquids. The heat and mass balancing characteristics were further characterized by the addition of Brownian motion and thermophoretic variables. The average entropy rate decreases as the magnetic factor and Brinkman number improves. Bilal *et al.* [20] addressed the micropolar NF flow over a vertically orientated, nonlinearly stretchy Riga surface, considering varying thermal conductivity and Brownian diffusion with the Levenberg–Marquardt back propagation technique. The flow rate was observed to increase when the Hartmann number, velocity slip, and buoyancy force parameters.

Mohanty *et al.* [21] evaluated the thermal and flow properties of a cross-ternary HNF flow consisting of single-walled carbon nanotubes, GO, and MWCNT NPs through a stretching cylinder.

Chemical reactions (CRs) and Arrhenius activation energy (AAE) play critical roles in fluid mathematical models, especially in processes including fluids that react during flow [22]. Studying the Arrhenius equation, which depicts the rate of CRs as exponentially dependent upon temperature, assists engineers to precisely model the behavior of products and reactants under various thermal scenarios. This is critical for improving reaction kinetics and the performance of reactors and transmission lines. In technologies such as catalytic converters, fluid dynamics combined with reaction kinetics aid in the design of more effective catalysts by disclosing how temperature affects reaction rates, hence assisting in pollutant removal [23]. Moreover, in biological processes, fluid models that incorporate CRs allow scholars to investigate complex phenomena such as the transfer of nutrients in fluids, resulting in advances in pharmaceuticals and biotechnology. Ultimately, incorporating CR kinetics and AAE into fluid models improves our knowledge and optimization of chemical processes in a variety of domains [24]. Ullah *et al.* [25] investigated the effect of melting heat exchange and AAE on an unstable Prandtl-Eyring model. It was concluded that the impact of AAE accelerates the fluid concentration field. Sudarmozhi *et al.* [26] evaluated the Maxwell double-diffusive convective fluid flow in the presence of CRs, heat radiation, and AAE on a perforated vibrating flat plate. It was discovered that as the heat formation rate increases, the temperature profile decreases, whereas the concentration profile diminishes with the variation in CRs factor. Some further related results are calculated in previous studies [27–30].

An investigation of the physical characteristics of NN-HNF comprising Al_2O_3 and CeO_2 NPs found that Al_2O_3 and CeO_2 NPs boosts the capability of designing structures as well as processes for an extensive variety of industry applications, thereby enhancing the product's durability and performance. Alumina NPs are widely recognized for their physical and thermal features. When preparing the HNF, empirical research to quantify thermal conductivity, viscosity, stability, and reliability is essential to govern the best combination for practical applications. Combining Al_2O_3 NPs with CeO_2 NPs, commonly referred to as cerium dioxide or cerium(IV) oxide, enhances viscosity and transference of heat, making it ideal for cooling and thermal systems. Therefore, in the current analysis, the NN-HNF flow including Al_2O_3 and CeO_2 NPs over a porous stretching or shrinking Riga sheet is studied. The flow phenomena are modeled in the form of nonlinear partial differential equations (PDEs), which are reduced into the dimension-free form through the similarity conversion. The solution is obtained by using the numerical approach parametric continuation method (PCM). The results are compared to the numerical outcomes of the published studies. In the coming sections, the flow is mathematically formulated and solved.

2 Mathematical formulation

An incompressible and steady 2D NN-HNF flow across a porous stretching or shrinking Riga sheet is studied. The HNF is synthesized by the scattering of CeO_2 and Al_2O_3 NPs. The Riga plate is stretching with velocity $u_w = ax$, toward the x direction, where a is considered to be constant as shown in Figure 1. Here T & C are the temperature and NN fluid concentration of NN HNF. The electromagnetic effect defined as $F_m = (F_m, 0,0) : \left[F_m = \exp\left(\frac{\pi M_0 j_0}{8\rho_{nf}}\right)\left(-\frac{\pi}{c}y\right)\right]$ [31] is employed on the extending and dwindling surface. Based on the above assumptions, the flow is formulated as [32,33]

$$\frac{\partial u}{\partial x} + \frac{\partial v}{\partial y} = 0, \tag{1}$$

$$\begin{aligned} u\frac{\partial u}{\partial x} = {} & \frac{\mu_{hnf}}{\rho_{hnf}}\frac{\partial^2 u}{\partial y^2} + \frac{\pi j_0 x M_0}{8\rho_{hnf}}\exp\left(-\frac{\pi}{c}y\right) - \frac{\nu_{hnf}}{K}u - v\frac{\partial u}{\partial y} \\ & \pm \frac{1}{\rho_{hnf}}\frac{x}{\upsilon_{hnf}}\left(\frac{\partial^3 u}{\partial x \partial y^2} - \frac{\partial^3 u}{\partial y^2 \partial x} + u\frac{\partial^3 u}{\partial x \partial y^2} \right. \\ & \left. + v\frac{\partial^3 u}{\partial y^3}\right], \end{aligned} \tag{2}$$

$$\begin{aligned} u\frac{\partial T}{\partial x} + v\frac{\partial T}{\partial y} = {} & \frac{k_{hnf}}{(\rho C_p)_{hnf}}\frac{\partial^2 T}{\partial y^2} - \frac{1}{(\rho C_p)_{hnf}}\frac{\partial q_r}{\partial y} \\ & + \frac{Q_e^*}{(\rho C_p)_{hnf}}(T - T_\infty)\exp\left(-\sqrt{\frac{a}{\upsilon_f}}ny\right), \end{aligned} \tag{3}$$

$$\begin{aligned} u\frac{\partial C}{\partial x} + v\frac{\partial C}{\partial y} = {} & D_{hnf}\frac{\partial^2 C}{\partial y^2} - \frac{\partial}{\partial y}(V_T(C - C_\infty)) \\ & - k_r(C - C_0)\left(\frac{T}{T_\infty}\right)^n \exp\left(\frac{-E_e}{kT}\right). \end{aligned} \tag{4}$$

Here V_T is the thermophoretic velocity and q_r is the heat radiation, which are defined as

$$V_T = -\frac{k_{vf}}{T_r}(T_w - T_\infty), \; q_r = -\frac{4\sigma}{3k}\left(\frac{\partial T^4}{\partial y}\right). \tag{5}$$

The boundary conditions (BCs) for Eqs. (2)–(4) are introduced as

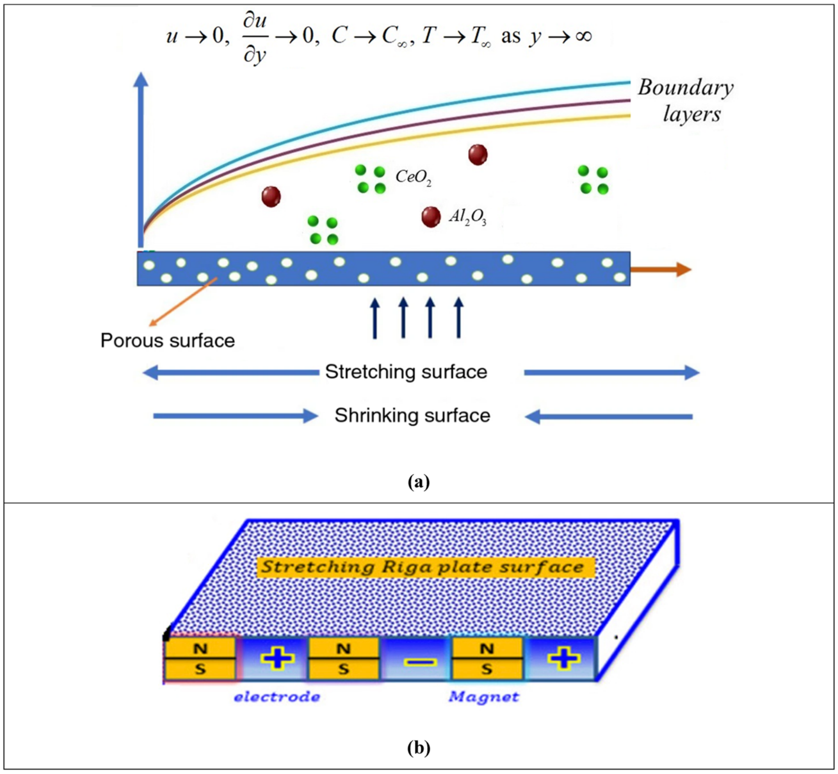

Figure 1: Graphical sketch of NN-HNF flow (a) and stretching sheet (Riga sheet) (b).

$$\left.\begin{aligned} &u = \lambda u_{\mathrm{w}},\ v = 0,\ T = T_{\mathrm{w}},\ C = C_{\mathrm{w}} \text{ at } y = 0 \\ &u \to 0,\ \frac{\partial u}{\partial y} \to 0,\ C \to C_\infty,\ T \to T_\infty \text{ as } y \to \infty \end{aligned}\right\}. \tag{6}$$

The similarity variables are introduced as

$$\left.\begin{aligned} &u = xaf',\ v = -\sqrt{a\nu_{\mathrm{f}}}\, f,\ \theta = \frac{T - T_\infty}{T_{\mathrm{w}} - T_\infty},\ \varphi = \frac{C - C_\infty}{C_{\mathrm{w}} - C_\infty}, \\ &\psi = x\sqrt{a\nu_{\mathrm{f}}}\, f,\ \eta = \sqrt{\frac{a}{\nu_{\mathrm{f}}}}\, y. \end{aligned}\right\} \tag{7}$$

where M_0 and k_{r} are the magnetization and the rate of CR, E_a and K are the activation energy and surface permeability, λ presents the stretching and dwindling velocity of the sheet, ($\lambda < 0$ is the shrinking case and $\lambda > 0$ is the stretching case), $\alpha_1 > 0$ indicates the SG fluid and $\alpha_1 < 0$ shows the Walter's B fluid, c and j_0 are the electrode width and current density of electrode current, respectively.

By substituting Eq. (7) in Eqs. (1)–(4), (6), we obtain

$$\begin{aligned} &\frac{f'''}{\vartheta_1\vartheta_2} \pm \frac{K_1}{\vartheta_2}[2f'f''' - ff'''' - (f'')^2] + \frac{Q_{\mathrm{h}}}{\vartheta_2}\exp(-\eta\beta_1) \\ &\quad - \frac{\lambda_1}{\vartheta_1\,\vartheta_2} f' + ff'' - (f')^2 = 0, \end{aligned} \tag{8}$$

$$\begin{aligned} &\left(\frac{k_{\mathrm{hnf}}}{k_{\mathrm{f}}} + \frac{4}{3}\mathrm{Rd}\right)\left(\frac{1}{\Pr\,\vartheta_3}\right)\theta'' + \vartheta_3 f(\eta)\theta'(\eta) + Q_e\exp(-n\eta) \\ &\quad = 0, \end{aligned} \tag{9}$$

$$\begin{aligned} &\phi'' + S_{\mathrm{c}}\, f\phi' - \tau\, S_{\mathrm{c}}(\theta''\phi + \theta'\phi') - S_{\mathrm{c}}\, K_{\mathrm{r}}(1 + \delta\theta)e^{\left(\frac{-E_{\mathrm{a}}}{(1+\delta\theta)}\right)}\phi \\ &\quad = 0. \end{aligned} \tag{10}$$

The BCs are

$$\left.\begin{aligned} &f(\eta) = 0,\ f'(\eta) = \lambda,\ \theta(\eta) = 1,\ \phi(\eta) = 1,\ \text{at } \eta = 0 \\ &f'(\eta) = 0,\ \theta(\eta) = 0,\ \phi(\eta) = 0,\ \text{as } \eta \to \infty \end{aligned}\right\}. \tag{11}$$

Table 1: Numerical values of thermophysical properties [33]

Materials	Density ρ (kg m^{-3})	Heat capacitance C_{p} (J kg^{-1}K^{-1})	Thermal conductivity k (kg ms^{-3}K^{-1})	Size (nm)
Sodium alginate SA($C_6H_9NaO_7$)	989	4,175	0.6376	—
Al_2O_3	3,970	765	46	10–100
CeO_2	7.2	600	22	5–50

where $K_1 < 0$ elaborates the Walter's B fluid, while $K_1 > 0$ is the SG fluid.

In Tables 1 and 2, ρ is the density, C_p is the heat capacity, ρC_p is the thermal capacity and σ is the electrical conductivity, where ϑ_1, ϑ_2, and ϑ_3 are defined as

$$\left.\begin{aligned}\vartheta_1 &= \frac{1}{(1-\phi_{Al_2O_3}-\phi_{CeO_2})^{2.5}},\\ \vartheta_2 &= \phi_{Al_2O_3}\left(\frac{\rho_{Al_2O_3}}{\rho_{bf}}\right)+\phi_{CeO_2}\left(\frac{\rho_{CeO_2}}{\rho_{bf}}\right)\\ &\quad +(1-\phi_{Al_2O_3}-\phi_{CeO_2}),\\ \vartheta_3 &= \phi_{Al_2O_3}\left(\frac{(\rho C_p)_{Al_2O_3}}{(\rho C_p)_{bf}}\right)+\phi_{CeO_2}\left(\frac{(\rho C_p)_{CeO_2}}{(\rho C_p)_{bf}}\right)\\ &\quad +(1-\phi_{Al_2O_3}-\phi_{CeO_2}).\end{aligned}\right. \tag{12}$$

In above equations, $K_1 = \frac{\alpha_1 a}{\rho_f \nu_f}$ is the viscoelastic factor, $\tau = \frac{-K(T_w - T_\infty)}{T_r}$ is the thermophoretic parameter, $Q_h = \frac{\pi j_0 M_0}{8\rho_f a U_w}$ is the modified Hartmann number, $\text{Rd} = \frac{4\sigma T_\infty^3}{kk_f}$ is the thermal radiation term, $E_a = \frac{E_e}{\kappa T_\infty}$ is the factor of activation energy, $\delta^* = \frac{D_B}{D_A}$ is the diffusion coefficient of mass, $K_r = \frac{k_r^2}{c}$ shows the rate of CR, $\beta_1 = \sqrt{\frac{\pi^2 \nu_f}{c^2 a}}$ is the magnitude and width of electrodes, $S_c = \left(\frac{\upsilon_f}{D_f}\right)$ is the Schmidt number, $\lambda_1 = \frac{\nu_f}{Ka}$ is the porosity factor, $Q_e = \frac{Q_e^* l}{a(\rho C_p)_f}$ is the heat source/sink factor, $\text{Re} = \frac{x^2 a}{\nu_f}$ is the Reynolds number, and $\text{Pr} = \frac{\nu_f}{\alpha_f}$ is the Prandtl number.

The physical interest quantities, such as Nusselt number and skin friction are stated as [31]

$$\left.\begin{aligned}\text{Nu} &= -\frac{x(k_{hnf}+16\sigma T_\infty^3/3k)}{(T_w - T_\infty)k_f}\left(\frac{\partial T}{\partial y}\right)_{y=0},\\ \text{Sh} &= -\frac{xD_f}{(C_w - C_\infty)D_f}\left(\frac{\partial C}{\partial y}\right)_{y=0},\\ \text{Cf} &= \frac{1}{U_w^2\rho_f}\left(\mu_{hnf}\frac{\partial u}{\partial y} \pm \alpha_1\left(v\frac{\partial^2 u}{\partial y^2}+\frac{\partial^2 u}{\partial x\partial y}u + 2\frac{\partial^2 u}{\partial x \partial y}\right)\right)_{y=0}.\end{aligned}\right\} \tag{13}$$

By inserting Eq. (6) in Eq. (13), we obtain

$$\left.\begin{aligned}&\text{Nu} = -\left(k_{hnf}/k_f + \frac{4}{3}\text{Rd}_1\right)\theta'(0)\sqrt{\text{Re}}, \quad \frac{\text{Sh}}{\sqrt{\text{Re}}} = -\varphi'(0),\\ &\text{Cf} = -\frac{1}{\sqrt{\text{Re}}}\left(f'''(0)K_1 f(0) - \left(\frac{1}{\vartheta_1} \pm 3(K_1)f'(0)\right)f''(0)\right).\end{aligned}\right\} \tag{14}$$

3 Stability analysis

Considering that there are multiple solutions to a physical model *vs* one parameter makes it necessary to assess the physical validity of each solution. The stability evaluations could be useful in applications related to engineering. In this way, we investigate the stability of dual solutions. As a result, an additional variable relating to the beginning value problem is appropriate for determining which solution will be obtained in actuality.

Therefore, we recall Eqs. (2), (3), (6), and (7) as (Weidman *et al.* [34] and Merkin [35])

Table 2: Thermal properties of HNF ($\phi_1 = \phi_{Al_2O_3}$, $\phi_2 = \phi_{CeO_2}$)

Properties	Al_2O_3–CeO_2/WEG
Viscosity	$\frac{\mu_{hnf}}{\mu_{bf}} = \frac{1}{(1-\phi_{Al_2O_3}-\phi_{CeO_2})^2}$
Density	$\frac{\rho_{hnf}}{\rho_{bf}} = \phi_{Al_2O_3}\left(\frac{\rho_{Al_2O_3}}{\rho_{bf}}\right)+\phi_{CeO_2}\left(\frac{\rho_{CeO_2}}{\rho_{bf}}\right)+(1-\phi_{Al_2O_3}-\phi_{CeO_2})$
Thermal capacity	$\frac{(\rho C_p)_{hnf}}{(\rho C_p)_{bf}} = \phi_{Al_2O_3}\left(\frac{(\rho C_p)_{Al_2O_3}}{(\rho C_p)_{bf}}\right)+\phi_{CeO_2}\left(\frac{(\rho C_p)_{CeO_2}}{(\rho C_p)_{bf}}\right)+(1-\phi_{Al_2O_3}-\phi_{CeO_2})$
Thermal conductivity	$\frac{k_{hnf}}{k_{bf}} = \left[\frac{\left(\frac{\phi_{Al_2O_3}k_{Al_2O_3}+\phi_{CeO_2}k_{CeO_2}}{\phi_{Al_2O_3}+\phi_{CeO_2}}\right)+2k_{bf}+2(\phi_{Al_2O_3}k_{Al_2O_3}+\phi_{CeO_2}k_{CeO_2})-2(\phi_{Al_2O_3}+\phi_{CeO_2})k_{bf}}{\left(\frac{\phi_{Al_2O_3}k_{Al_2O_3}+\phi_{CeO_2}k_{CeO_2}}{\phi_{Al_2O_3}+\phi_{CeO_2}}\right)+2k_{bf}-2(k_{Al_2O_3}\phi_{Al_2O_3}+k_{CeO_2}\phi_{CeO_2})+(\phi_{Al_2O_3}+\phi_{CeO_2})2k_{bf}}\right]$
Electrical conductivity	$\frac{\sigma_{hnf}}{\sigma_{bf}} = \left[\frac{\left(\frac{\phi_{Al_2O_3}\sigma_{Al_2O_3}+\sigma_{CeO_2}\phi_{CeO_2}}{\phi_{CeO_2}+\phi_{Al_2O_3}}\right)+2\sigma_{bf}+2(\sigma_{Al_2O_3}\phi_{Al_2O_3}+\sigma_{CeO_2}\phi_{CeO_2})-2(\phi_{CeO_2}+\phi_{Al_2O_3})\sigma_{bf}}{\left(\frac{\phi_{Al_2O_3}\sigma_{Al_2O_3}+\phi_{CeO_2}\sigma_{CeO_2}}{\phi_{Al_2O_3}+\phi_{CeO_2}}\right)+2\sigma_{bf}-(\sigma_{Al_2O_3}\phi_{Al_2O_3}+\sigma_{CeO_2}\phi_{CeO_2})+(\phi_{CeO_2}+\phi_{Al_2O_3})\sigma_{bf}}\right]$

$$\frac{\partial u}{\partial t} + u\frac{\partial u}{\partial x} = \frac{\mu_{\text{hnf}}}{\rho_{\text{hnf}}}\frac{\partial^2 u}{\partial y^2} + \frac{\pi j_0 x M_0}{8\rho_{\text{hnf}}}\exp\left(-\frac{\pi}{c}y\right) - \frac{\nu_{\text{hnf}}}{K}u - v\frac{\partial u}{\partial y} \pm \frac{1}{\rho_{\text{hnf}}}\frac{x}{\upsilon_{\text{hnf}}}\left(\begin{array}{c}\frac{\partial^3 u}{\partial x \partial y^2} - \frac{\partial^3 u}{\partial y^2 \partial x} + \\ u\frac{\partial^3 u}{\partial x \partial y^2} + v\frac{\partial^3 u}{\partial y^3}\end{array}\right), \tag{15}$$

$$u\frac{\partial T}{\partial x} + v\frac{\partial T}{\partial y} = \frac{k_{\text{hnf}}}{(\rho C_{\text{p}})_{\text{hnf}}}\frac{\partial^2 T}{\partial y^2} - \frac{1}{(\rho C_{\text{p}})_{\text{hnf}}}\frac{\partial q_{\text{r}}}{\partial y} + \frac{Q_{\text{e}}^*}{(\rho C_{\text{p}})_{\text{hnf}}}(T - T_\infty)\exp\left(-\sqrt{\frac{a}{\upsilon_{\text{f}}}}ny\right), \tag{16}$$

The similarity variables are also modified as

$$\left.\begin{array}{l}\eta = \sqrt{\frac{a}{\nu_{\text{f}}}}y,\ u = xaf'(\eta,\tau),\ v = -\sqrt{a\nu_{\text{f}}}f(\eta,\tau),\\ \varphi(\eta,\tau) = \frac{C - C_\infty}{C_{\text{w}} - C_\infty},\ \theta(\eta,\tau) = \frac{T - T_\infty}{T_{\text{w}} - T_\infty},\\ \psi = x\sqrt{a\nu_{\text{f}}}f(\eta,\tau),\ \tau = at.\end{array}\right\} \tag{17}$$

By employing Eq. (17) in Eqs. (15) and (16)

$$\frac{1}{\vartheta_1\vartheta_2}\left(\frac{\partial^3 f}{\partial\eta^3}\right) \pm \frac{K_1}{\vartheta_2}\left[2\frac{\partial f}{\partial\eta}\left(\frac{\partial^3 f}{\partial\eta^3}\right) - \frac{\partial f}{\partial\eta}\left(\frac{\partial^4 f}{\partial\eta^4}\right) - \left(\frac{\partial^2 f}{\partial\eta^2}\right)^2\right] + \frac{Q_{\text{h}}}{\vartheta_2}\exp(-\eta\beta_1) - \frac{\lambda_1}{\vartheta_1\vartheta_2}\left(\frac{\partial f}{\partial\eta}\right) + \frac{\partial f}{\partial\eta}\left(\frac{\partial^2 f}{\partial\eta^2}\right) - \left(\frac{\partial f}{\partial\eta}\right)^2 - \frac{\partial^2 f}{\partial\eta\partial\tau} = 0, \tag{18}$$

$$\left(\frac{k_{\text{hnf}}}{k_{\text{f}}} + \frac{4}{3}\text{Rd}\right)\left(\frac{1}{\Pr\vartheta_3}\right)\frac{\partial^2\theta}{\partial\eta^2} + \frac{\partial f}{\partial\eta}\left(\frac{\partial\theta}{\partial\eta}\right) + Q_{\text{e}}\exp(-n\eta) - \left(\frac{\partial\theta}{\partial\tau}\right) = 0. \tag{19}$$

Similarly, the BCs are also modified as

$$\left.\begin{array}{l}f'(0,\tau) = \lambda,\ f(0,\tau) = 0,\ \theta(0,\tau) = 1,\ \text{at}\ \eta = 0\\ f'(\eta,\tau) = 0,\ \theta(\eta,\tau) = 0,\ \text{as}\ \eta\to\infty\end{array}\right\}. \tag{20}$$

Consider, $f(\eta) = f_0(\eta)$ & $\theta(\eta) = \theta_0(\eta)$ in order to check the stability of Eqs. (8) and (9). The succeeding terms satisfying the main model as (Merrill *et al.* [36] and Weidman and Sprague [37])

$$\left.\begin{array}{l}\theta(\eta,\tau) = \theta_0(\eta) + \text{e}^{-\gamma\tau}H(\eta),\\ f(\eta,\tau) = f_0(\eta) + e^{-\gamma\tau}F(\eta).\end{array}\right\} \tag{21}$$

Here $H(\eta)$ and $F(\eta)$ are very small as compared to $\theta_0(\eta)$ and $f_0(\eta)$, where γ is the small eigenvalue that we shall calculate.

By inserting Eq. (21) in Eqs. (18) and (19), we obtain

$$\frac{1}{\vartheta_1\vartheta_2}\left(\frac{\partial^3 F}{\partial\eta^3}\right) \pm \frac{K_1}{\vartheta_2}\left[2\frac{\partial F}{\partial\eta}\left(\frac{\partial^3 F}{\partial\eta^3}\right) - \frac{\partial F}{\partial\eta}\left(\frac{\partial^4 F}{\partial\eta^4}\right) - \left(\frac{\partial^2 F}{\partial\eta^2}\right)^2\right] + \frac{Q_{\text{h}}}{\vartheta_2}\exp(-\eta\beta_1) - \frac{\lambda_1}{\vartheta_1\vartheta_2}\frac{\partial F}{\partial\eta} + \frac{\partial F}{\partial\eta}\left(\frac{\partial^2 F}{\partial\eta^2}\right) + Ff'' + (\gamma - 2f'_0)\left(\frac{\partial F}{\partial\eta}\right) = 0, \tag{22}$$

$$\left(\frac{k_{\text{hnf}}}{k_{\text{f}}} + \frac{4}{3}\text{Rd}\right)\left(\frac{1}{\Pr\vartheta_3}\right)\frac{\partial^2 H}{\partial\eta^2} + \frac{\partial F}{\partial\eta}\left(\frac{\partial H}{\partial\eta}\right) + Q_{\text{e}}\exp(-n\eta) + \gamma(H) = 0. \tag{23}$$

$$\left.\begin{array}{l}F(0) = 0,\ \frac{\partial F(0)}{\partial\eta} = 0,\ H(0) = 0,\ \text{at}\ \eta = 0\\ \frac{\partial F(0)}{\partial\eta}\to 0,\ H(\eta)\to 0,\ \text{as}\ \eta\to\infty\end{array}\right\}. \tag{24}$$

Consider, $\tau = 0$, for the stability of the steady-state flow solutions.

$$\frac{1}{\vartheta_1\vartheta_2}(F'''_0) \pm \frac{K_1}{\vartheta_2}[2F'''_0F'_0 - F'_0F_0^{\text{iv}} - (F''_0)^2] + \frac{Q_{\text{h}}}{\vartheta_2}\exp(-\eta\beta_1) - \frac{\lambda_1}{\vartheta_1\vartheta_2}F'_0 + F_0F''_0 + F'_0F''_0 + (\gamma - 2f'_0)F'_0 = 0, \tag{25}$$

$$\left(\frac{k_{\text{hnf}}}{k_{\text{f}}} + \frac{4}{3}\text{Rd}\right)\left(\frac{1}{\Pr\vartheta_3}\right)H''_0 + H'_0F'_0 + Q_{\text{e}}\exp(-n\eta) + \gamma(H_0) = 0. \tag{26}$$

$$\left.\begin{array}{l}F_0(0) = 0,\ F'_0 = 0,\ H_0(0) = 0,\ \text{at}\ \eta = 0\\ F'_0(\eta)\to 0,\ H_0(\eta)\to 0,\ \text{as}\ \eta\to\infty\end{array}\right\}. \tag{27}$$

To derive the eigenvalues, we keep $F'_0(\eta)\to 0$, as $\eta\to\infty$ as (Harris *et al.* [38]). Moreover, the current work demonstrated the presence of non-uniqueness solutions within a confined range of the shrinkage factor, but a unique solution was established in that stretching case. The stability study found that the first solution has an extremely small positive eigenvalue, indicating that it was both stable and practicable.

4 Numerical solution

The PCM is a powerful tool used in mathematical computation along with various applied sciences to study how equation solutions modify when parameter varies. Here are a few notable applications of PCM, for example, it is frequently employed for investigating bifurcations in dynamical systems, fluid mechanics, engineering mechanical systems, control optimization problems, mathematical geometry, machine learning, computation in the field of neuroscience, and both dynamic and static system modelling. These applications highlight the adaptability and utility of PCM in a range of study subjects and technical domains, making it an invaluable tool for researchers analyzing systems with complex behaviors [39,40]. To employ the PCM, the following phases are used:

Step 1: Reduction of order

$$\begin{aligned} &f = \varpi_1(\eta),\ f' = \varpi_2(\eta),\ f'' = \varpi_3(\eta),\ \theta = \varpi_4(\eta),\\ &\theta' = \varpi_5(\eta),\ \phi = \varpi_6(\eta),\ \phi' = \varpi_7(\eta). \end{aligned} \tag{28}$$

By inserting Eq. (28) in Eqs. (8)–(11) and (12), we obtain

$$\begin{aligned} &\frac{\varpi'_3(\eta)}{\vartheta_1\vartheta_2} \pm \frac{K_1}{\vartheta_2}[2\varpi_2(\eta)\varpi'_3(\eta) - \varpi_1(\eta)\varpi'_3(\eta)\\ &\quad - (\varpi_3(\eta))^2] + \frac{Q_1}{\vartheta_2}\exp(-\eta\beta_1) - \frac{\lambda_1}{\vartheta_1\vartheta_2}\varpi_2(\eta)\\ &\quad + \varpi_1(\eta)\varpi_2(\eta) - (\varpi_2(\eta))^2 = 0, \end{aligned} \tag{29}$$

$$\begin{aligned} &\left(\frac{k_{\mathrm{hnf}}}{k_{\mathrm{f}}} + \frac{4}{3}\mathrm{Rd}\right)\left(\frac{1}{\mathrm{Pr}\ \vartheta_3}\right)\varpi'_5 + \vartheta_3\varpi_1(\eta)\varpi_5(\eta)\\ &\quad + Q_{\mathrm{e}}\exp(-n\eta) = 0, \end{aligned} \tag{30}$$

$$\begin{aligned} &\varpi'_7 + S_{\mathrm{c}}\ \varpi_1\varpi_7 - \tau S_{\mathrm{c}}(\varpi'_5\varpi_6 + \varpi_5\ \varpi_7)\\ &\quad - S_{\mathrm{c}}\ K_{\mathrm{r}}(1 + \delta\ \varpi_4)e^{\left(\frac{-E_{\mathrm{a}}}{(1+\delta\varpi_4)}\right)}\varpi_6 = 0. \end{aligned} \tag{31}$$

The BCs are

$$\left.\begin{aligned} &\varpi_1(\eta) = 0,\ \varpi_2(\eta) = \lambda,\ \varpi_4(\eta) = 1,\ \varpi_6(\eta) = 1,\\ &\text{at } \eta = 0\\ &\varpi_2(\eta) = 0,\ \varpi_4(\eta) = 0,\ \varpi_6(\eta) = 0,\ \text{as } \eta \to \infty \end{aligned}\right\}. \tag{32}$$

Step 2: Introducing parameter "*p*"

$$\left.\begin{aligned} &\left(\frac{1}{\vartheta_1\vartheta_2}\right)\varpi'_3(\eta) \pm \frac{K_1}{\vartheta_2}[2\varpi_2(\eta)\varpi'_3(\eta) - \varpi_1(\eta)\varpi'_3(\eta)\\ &\quad - p(\varpi_3(\eta) - 1)^2] + \frac{Q_1}{\vartheta_2}\exp(-\eta\beta_1) - \frac{\lambda_1}{\vartheta_1\vartheta_2}\\ &\varpi_2(\eta) + \varpi_1(\eta)\varpi_2(\eta) - (\varpi_2(\eta))^2 = 0 \end{aligned}\right\}, \tag{33}$$

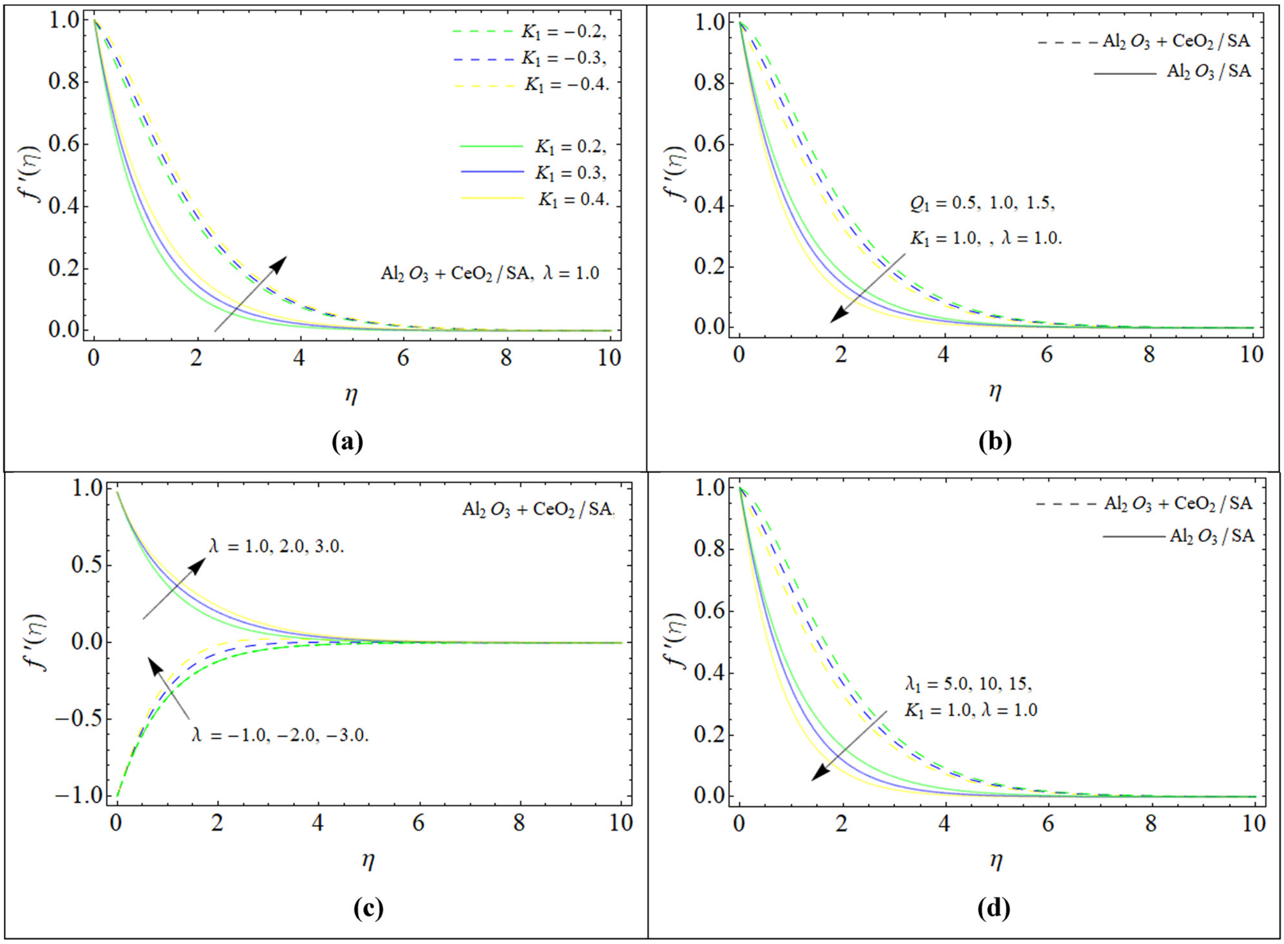

Figure 2: NN-HNF velocity profile $f'(\eta)$ *vs* (a) viscoelastic factor K_1, (b) modified Hartmann number Q_1, (c) stretching/shrinking surface factor, and (d) porous surface parameter λ_1.

$$\left(\frac{k_{\mathrm{hnf}}}{k_{\mathrm{f}}} + \frac{4}{3}\mathrm{Rd}\right)\left(\frac{1}{\Pr \vartheta_3}\right)\varpi'_5 + \vartheta_3\, \varpi_1(\eta)(\varpi_5(\eta) - 1)p + Q_{\mathrm{e}} \exp(-n\eta) = 0, \tag{34}$$

$$\varpi'_7 + S_{\mathrm{c}}\, \varpi_1(\varpi_7 - 1)p - \tau S_{\mathrm{c}}(\varpi'_5\varpi_6 + \varpi_5\varpi_7) - S_{\mathrm{c}}K_{\mathrm{r}}(1 + \delta\, \varpi_4)e^{\left(\frac{-E_{\mathrm{a}}}{(1+\delta\varpi_4)}\right)}\varpi_6 = 0. \tag{35}$$

The BCs remained the same as

$$\left.\begin{array}{l} \varpi_1(\eta) = 0,\ \varpi_2(\eta) = \lambda,\ \varpi_4(\eta) = 1,\ \varpi_6(\eta) = 1, \\ \text{at } \eta = 0 \\ \varpi_2(\eta) = 0,\ \varpi_4(\eta) = 0,\ \varpi_6(\eta) = 0,\ \text{as } \eta \to \infty \end{array}\right\}. \tag{36}$$

Step 3: By using the implicit scheme as

$$\frac{U^{i+1} - U^{i}}{\Delta\eta} = AU^{i+1} \text{ and } \frac{W^{i+1} - W^{i}}{\Delta\eta} = AW^{i+1}. \tag{37}$$

Finally, we obtain the iterative form:

$$U^{i+1} = \frac{U^{i}}{(I - \Delta\eta A)} \text{ and } W^{i+1} = \frac{(W^{i} + \Delta\eta R)}{(I - \Delta\eta A)}. \tag{38}$$

5 Results and discussion

In the current analysis, the NN-HNF flow including Al_2O_3 and CeO_2 NPs over a porous stretching or shrinking Riga sheet is studied. The flow phenomena are modeled in the form of nonlinear PDEs, which are reduced into the dimension-free form through the similarity conversion. The solution is obtained by using the numerical approach PCM. The results are compared to the numerical outcomes of the published studies.

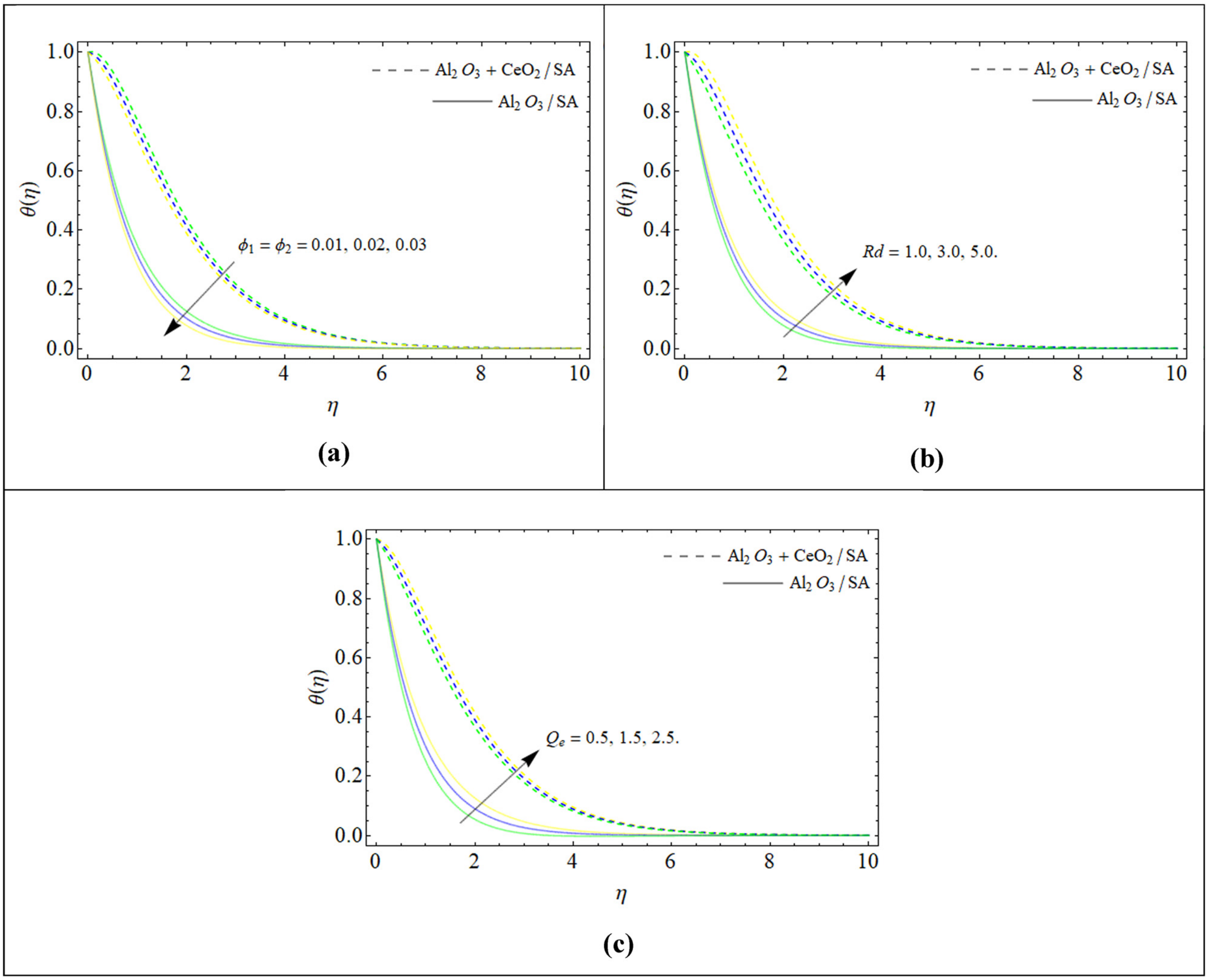

Figure 3: Thermal profile $\theta(\eta)$ *vs* the variation in (a) CeO_2 and Al_2O_3 NPs, (b) heat radiation Rd, and (c) exponential heat source/sink Q_e.

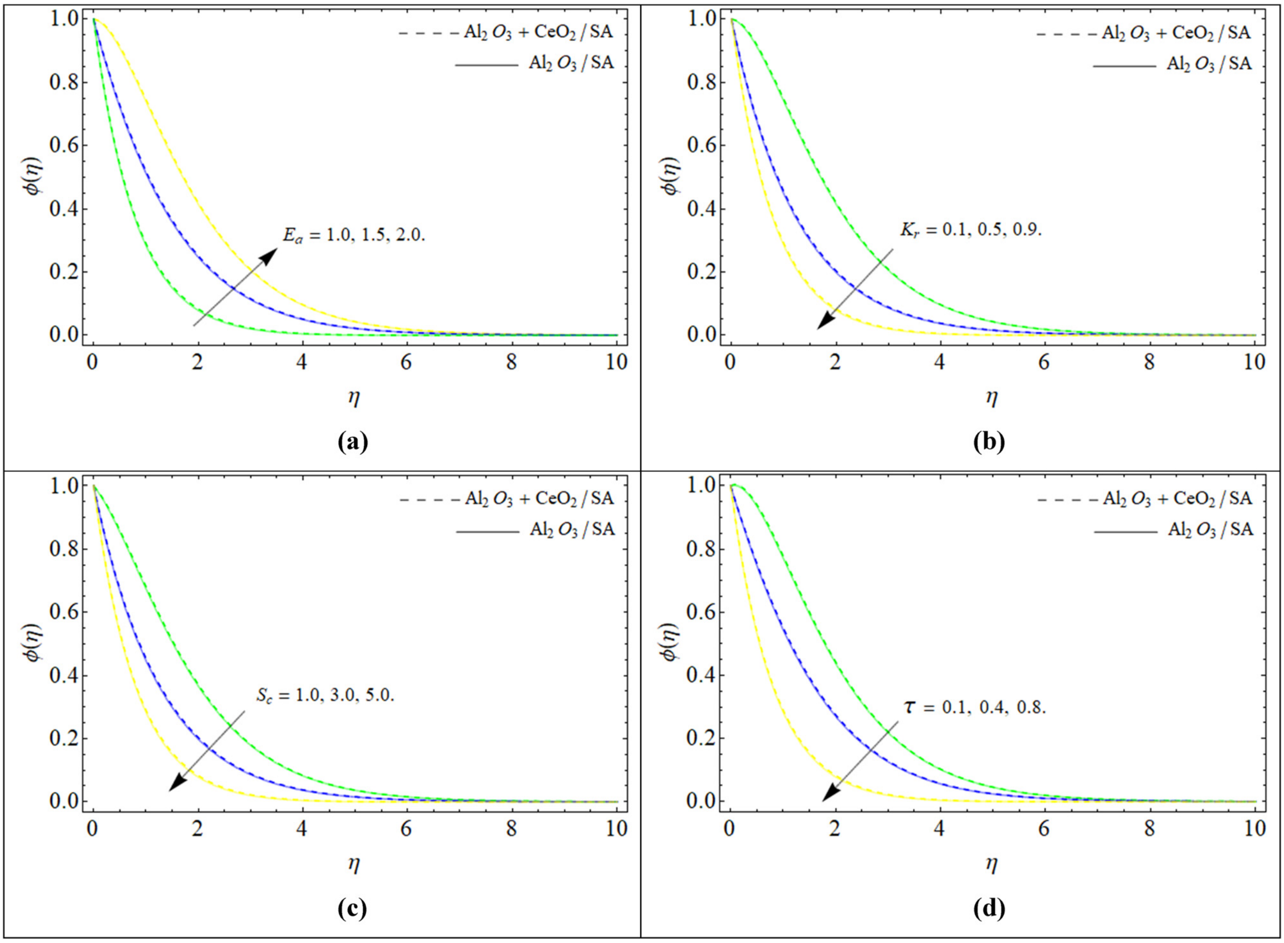

Figure 4: Fluid concentration distribution $\phi(\eta)$ *vs* (a) activation energy E_a, (b) CR K_r, (c) Schmidt number S_c, and (d) thermophoretic τ velocity factor.

Figure 2(a)–(d) reveal the variation in NN-HNF velocity profile $f'(\eta)$ *vs* viscoelastic factor K_1, modified Hartmann number Q_1, stretching/shrinking surface factor, and porous surface parameter λ_1 respectively. Figure 2(a) shows the impact of a viscoelastic factor K_1 on the velocity field of HNF (Al_2O_3 and CeO_2/SA) for the stretching case ($\lambda = 1.0$). It can be seen that the flow rate boosted in both cases (SG fluid $K_1 > 0$ and Walter's B fluid $K_1 < 0$). Physically, the increased fluid velocity in SG fluids and WB fluids is mostly owing to their viscoelastic character, which allows for flow adaptation, reduced effective viscosity by shear-thinning behaviors, and their capability to accumulate and utilize elastic energy. This combination produces much better flow properties than Newtonian fluids, which eventually contribute to higher fluid velocity under varied situations. Figure 2(b) demonstrates the impact of Q_1 on the velocity profile for SG fluid over a strehing sheet ($\lambda = 1.0$). It can be seen that the fluid velocity declines with the variation in Q_1. Physically, as the Q_1 rises, the magnetic effect on the fluid flow gets stronger, resulting in a phenomenon known as MHD damping. When a magnetic field is placed orthogonal to the flow direction, it creates Lorentz forces that act against the velocity of the fluid. These forces increase with the strength of the magnetic field, which efficiently resists the fluid's movement. As a result, larger Q_1 indicates increasing magnetic resistance, resulting in a considerable decline in fluid velocity. Figure 2(c) shows that the velocity curve is enhanced with the impact of λ. Fluid velocity increases as the sheet stretches and shrinks due to a direct effect of surface mobility at the boundary. Stretching a sheet improves the surface area that comes in contact with the fluid, causing a suction effect to entrain and accelerate the fluid around it. Stretching diminishes the thickness of the boundary layer, resulting in larger velocity gradients and enhanced shear stress, propelling the fluid further away from the surface. In contrast, a shrinking sheet can draw fluid toward itself, raising local velocity as fluid is drawn in. Thus, stretching and shrinking movements alter momentum transfer and flow properties, resulting in higher fluid velocity. Figure 2(d) illustrates

Table 3: Results validation against the published studies Madhukesh *et al.* [31], Abolbashari *et al.* [41], and Das *et al.* [42]

Pr	Madhukesh *et al.* [31]	Abolbashari *et al.* [41]	Das *et al.* [42]	Present work	Absolute percent error (%)
0.7	0.8087615	0.8085313	0.808751	0.8087674	0.00202
1.0	1.0000000	1.0000000	1.000000	1.0000000	0.00000
3.0	1.9235743	1.9236824	1.923573	1.9235856	0.00065
7.0	3.0731463	3.0722503	3.073146	3.0731632	0.00055
10	3.7206733	3.7206738	3.720673	3.7206903	0.00046

the effect of the permeability parameter on the velocity field. Physically, increasing values of λ_1 reduces the fluid velocity due to the resistance applied to the flow field. The pores increase the surface area for the HNF flow, thus when the fluid travels through pores with a larger surface area, it generates friction and so reduces fluid velocity.

Figure 3(a)–(c) displays the variation in thermal profile $\theta(\eta)$ *vs* the variation in CeO_2 and Al_2O_3 NPs, heat radiation Rd, and exponential heat source/sink Q_e. Figure 3(a) shows that the energy curve of NF and HNF both diminishes with the addition of CeO_2 and Al_2O_3 NPs. The addition of CeO_2 and Al_2O_3 NPs to a fluid reduces the fluid temperature due to the increased thermal conductivity and efficient heat transfer capabilities of these NPs. As the NPs spread in the fluid, they increase surface area for transferring heat as well as enhance thermal interactions between fluid molecules. CeO_2 and Al_2O_3 NPs have higher thermal conductivity than the base fluid, allowing them to absorb and distribute heat more effectively. Furthermore, the inclusion of NPs can destabilize the fluid's thermal boundary layer, allowing greater circulation and conduction of heat, which results in lower temperature relative to the unmodified fluid. Figure 3(b) shows that the energy field augments with the effect of Rd. Physically, Rd has the effect of increasing fluid temperature, mostly due to the inhalation of radiant energy from the source. In situations with high thermal radiation, particularly near a hot surface or in direct sunshine, the fluid absorbs infrared radiation, increasing its thermal energy. This absorption boosts the fluid's temperature as it accumulates energy, particularly when the fluid's emissivity is suitable for the effective absorption of heat. Similarly, the thermal field also enhances with the impact of Q_e as shown in Figure 3(c).

Figure 4(a)–(d) displays the variation in fluid concentration distribution $\phi(\eta)$ *vs* activation energy E_a, CR K_r, Schmidt number S_c, and thermophoretic velocity factor τ respectively. Figure 4(a) and (b) reveal that the effect of E_a enhances the $\phi(\eta)$, while the variation in K_r drops the fluid concentration. Physically, the impact of the E_a improves the fluid $\phi(\eta)$ because more activation energy is frequently associated with faster reaction rates and enhanced mass transmission in a fluid. When the activation energy of a CR increases, it usually takes more energy for the reactants to collide efficiently and transition into products. As the system temperature or energy inputs increase, so do the concentrations of reactive species, resulting in a greater concentration profile within the fluid. Furthermore, increased energy promotes molecular interactions and diffusion, which aids in the transportation of reactants and products across the fluid. As a result, the distribution of concentration increases steeply, which improves the $\phi(\eta)$. Figure 4(c) illustrates that the $\phi(\eta)$ drops with the impact of S_c. Physically, the kinetic viscosity of fluid increases with the variation in S_c, that is why the fluid concentration drops with the impact of S_c. Figure 4(d) also presents that the $\phi(\eta)$ declines with the effect of r. Physically, the $\phi(\eta)$ decreases with the effect of τ, because thermophoresis leads particles to move from high-temperature regions onto low-temperature regions, resulting in a reduction in the quantity of suspended particles in heated areas of the fluid. When the thermophoretic velocity is high, particles move in response to temperature gradients, effectively dispersing them from hotter, more concentrated zones. This migration causes a reduction in $\phi(\eta)$.

6 Results validation

Table 3 shows the numerical results validation against the published studies Madhukesh *et al.* [31], Abolbashari *et al.* [41], and Das *et al.* [42]. It has been determined that the current outcomes have the best resemblance with the published studies. The relative error between Das *et al.* [42] and present study at Pr = 10 is 0.00046%, which is gradually reduced up to 0.00202% with the variation of Pr = 0.7.

7 Conclusion

We have numerically examined the NN HNF flow comprising of Al_2O_3 and CeO_2 NPs over a porous stretching or shrinking Riga sheet. The flow phenomena are modeled in the form of nonlinear PDEs, which are reduced into the dimension free form through the similarity conversion. The solution is obtained by using the numerical approach PCM. The results are compared to the numerical outcomes of the published studies. The basic conclusions are as follows:

- The impact of a viscoelastic factor K_1 enhnaces the velocity field of HNF (Al_2O_3 and CeO_2/SA) in both cases (SG fluid $K_1 > 0$ and Walter's B fluid $K_1 < 0$) over a stretching sheet ($\lambda = 1.0$).
- The influence of Hartmann number Q_1 drops the velocity profile for SG fluid in case of stretching sheet ($\lambda = 1.0$).
- The fluid velocity increases with the impact of both stretching and shrinking of the Riga sheet.
- The effect of the surface permeability parameter drops the velocity field of both NF and HNF.
- The energy curve of NF and HNF diminishes with the addition of CeO_2 and Al_2O_3 NPs.
- The variation in heat radiation and exponential heat source/sink Q_e accelerates the thermal field of nano and HNF.
- The effect of activation energy E_a enhances the fluid concentration $\phi(\eta)$, while the variation in chemcial reaction factor K_r drops it.
- The fluid concentration profile $\phi(\eta)$ drops with the impact of S_c and thermophoretic velocity factor.
- The present model can be modified in future by considering other sorts of NN fluid over different geometries. It can be further extended by considering higher order slip conditions and other computational techniques.

Funding information: This study was supported *via* funding from Prince Sattam bin Abdulaziz University project number (PSAU/2025/R/1446).

Author contributions: H.Y. and A.S.: conceptualization and methodology; A.A.B., F.S.A. and A.S.: software, writing – original draft preparation; R.B. and A.A.B.: visualization and investigation; F.S.A., R.B., and H.Y.: validation and writing – reviewing and editing. All authors have contributed equally to this article. All authors have accepted responsibility for the entire content of this manuscript and approved its submission.

Conflict of interest: The authors state no conflict of interest.

Data availability statement: The datasets generated and/or analyzed during the current study are available from the corresponding author on reasonable request.

References

[1] González A, et al. Electrohydrodynamic flows induced by a Riga plate for microfluidic applications. Microfluid Nanofluid. 2018;22(5):1–12.
[2] Zhang X, et al. Enhanced heat transfer in a cooling system using a Riga plate. Int J Therm Sci. 2019;145:202–13.
[3] Davis RH, et al. Control of turbulence in industrial flows with electrohydrodynamic devices. Chem Eng Sci. 2020;226:115–26.
[4] Cui J, Razzaq R, Azam F, Farooq U, Hussain M, Chamkha AJ. Nonsimilar forced convection analysis of chemically reactive magnetized Eyring-Powell nanofluid flow in a porous medium over a stretched Riga surface. J Porous Media. 2022;25(10):67–81
[5] Algehyne EA, Saeed A, Arif M, Bilal M, Kumam P, Galal AM. Gyrotactic microorganism hybrid nanofluid over a Riga plate subject to activation energy and heat source: Numerical approach. Sci Rep. 2023;13(1):13675.
[6] Mohanty D, Mahanta G, Vajravelu K, Shaw S. Interfacial nanolayer mechanism and irreversibility analysis for nonlinear Arrhenius reactive hybrid nanofluid flow over an inclined stretched cylinder. Eur Phys J Plus. 2023;138(12):1–21.
[7] Farooq U, Akhtar K, Abbasi MM, Hussain M, Aldandani M. Convective heat transfer performance of MHD nanofluid flow with temperature dependent viscosity over stretching surface. ZAMM-J Appl Math Mech/Zeitschrift für Angewandte Mathematik und Mechanik. 2023;103(10):e202300053.
[8] Farooq U, Hussain M, Farooq U. Non-similar analysis of micropolar magnetized nanofluid flow over a stretched surface. Adv Mech Eng. 2024;16(4):16878132241233089.
[9] Bilal M, Hamad NH, AlQahtani SA, Pathak P. Numerical simulation of nanofluid flow across a slender stretching Riga plate subjected to heat source and activation energy. Numer Heat Transfer Part B: Fundam. 2024;86(7):2376–89.
[10] Xin X, Ganie AH, Alwuthaynani M, Bonyah E, El-Wahed Khalifa HA, Fathima D, et al. Parametric analysis of pollutant discharge concentration in non-Newtonian nanofluid flow across a permeable Riga sheet with thermal radiation. AIP Adv. 2024;14(4):045018
[11] Gangadhar K, Sangeetha Rani M, Wakif A. Improved slip mechanism and convective heat impact for ternary nanofluidic flowing past a riga surface. Int J Mod Phys B. 2025;39(8):2550064.
[12] Bilal M, Ullah S, Mostafa AM, AlQahtani NFA, Li S. Wastewater pollutant discharge concentration effect on non-Newtonian hybrid nanofluid flow across a Riga sheet: Numerical exploration. J Porous Media. 2025;28(1):1–17.
[13] Ahmadian A, Bilal M, Khan MA, Asjad MI. The non-Newtonian maxwell nanofluid flow between two parallel rotating disks under the effects of magnetic field. Sci Rep. 2020;10(1):1–14.
[14] Mohanty D, Mahanta G, Shaw S. Analysis of irreversibility for 3-D MHD convective Darcy–Forchheimer Casson hybrid nanofluid flow due to a rotating disk with Cattaneo–Christov heat flux, Joule heating, and nonlinear thermal radiation. Numer Heat Transfer Part B: Fundam. 2023;84(2):115–42.
[15] Mohanty D, Sethy N, Mahanta G, Shaw S. Impact of the interfacial nanolayer on Marangoni convective Darcy-Forchheimer hybrid nanofluid flow over an infinite porous disk with Cattaneo-Christov heat flux. Therm Sci Eng Prog. 2023;41:101854.
[16] Farooq U, Bibi A, Abbasi JN, Jan A, Hussain M. Nonsimilar mixed convection analysis of ternary hybrid nanofluid flow near

stagnation point over vertical Riga plate. Multidiscip Model Mater Struct. 2024;20(2):261–78.

[17] Cham A, Mustafa M. Exploring the dynamics of second-grade fluid motion and heat over a deforming cylinder or plate affected by partial slip conditions. Arab J Sci Eng. 2024;49(2):1505–14.

[18] Farooq U, Irfan M, Khalid S, Jan A, Hussain M. Computational convection analysis of second grade MHD nanofluid flow through porous medium across a stretching surface. ZAMM-J Appl Math Mech/Zeitschrift für Angewandte Mathematik und Mechanik. 2024;104(4):e202300401.

[19] Ahmad L, Abd-Elmonem A, Javed S, Yasir M, Khan U, Yilmaz Y, et al. Dissipative disorder analysis of Homann flow of Walters B fluid with the applications of solar thermal energy absorption aspects. Appl Water Sci. 2025;15(1):15.

[20] Bilal M, Maiz F, Farooq M, Ahmad H, Nasrat MK, Ghazwani HA. Novel numerical and artificial neural computing with experimental validation towards unsteady micropolar nanofluid flow across a Riga plate. Sci Rep. 2025;15(1):759.

[21] Mohanty D, Mahanta G, Shaw S. Irreversibility and thermal performance of nonlinear radiative cross-ternary hybrid nanofluid flow about a stretching cylinder with industrial applications. Powder Technol. 2024;433:119255.

[22] Janjua KH, Bilal M, Riaz MB, Saqib AB, Ismail EA, Awwad FA. Novel numerical approach toward hybrid nanofluid flow subject to Lorentz force and homogenous/heterogeneous chemical reaction across coaxial cylinders. AIP Adv. 2024;14(7):075129.

[23] Mohanty D, Mahanta G, Byeon H, Vignesh S, Shaw S, Khan MI, et al. Thermo-solutal Marangoni convective Darcy-Forchheimer bio-hybrid nanofluid flow over a permeable disk with activation energy: Analysis of interfacial nanolayer thickness. Open Phys. 2023;21(1):20230119.

[24] Bilal M, Farooq M, Benghanem M, Ahmad H. Entropy optimization in non-Newtonian Prandtl-Eyring fluid using ANN over a curved Riga surface. Int J Therm Sci. 2025;212:109765.

[25] Ullah Z, Ullah I, Zaman G, Sun TC. A numerical approach to interpret melting and activation energy phenomenon on the magnetized transient flow of Prandtl–Eyring fluid with the application of Cattaneo–Christov theory. Waves Random Complex Media. 2025;35(1):1351–71.

[26] Sudarmozhi K, Iranian D, Khan I. Chemical reaction effect across the moving flat plate with heat generation and MHD flow of Maxwell fluid with viscous dissipation. Int J Mod Phys B. 2025;39(3):2550027.

[27] Mohanty D, Mahanta G, Chamkha AJ, Shaw S. Numerical analysis of interfacial nanolayer thickness on Darcy-Forchheimer Casson hybrid nanofluid flow over a moving needle with Cattaneo-Christov dual flux. Numer Heat Transfer Part A: Appl. 2023;86(3):399–423.

[28] Farooq U, Hussain M, Farooq U. Non-similar analysis of chemically reactive bioconvective Casson nanofluid flow over an inclined stretching surface. ZAMM-J Appl Math Mech/Zeitschrift für Angewandte Mathematik und Mechanik. 2024;104(2):e202300128.

[29] Nadeem A, Khan SU, Bilal M, Saidani T, Jamshed W. Thermal augmentation in Darcy Forchheimer media flow using Extended Tiwari-Das model: Solar radiation aspects. J Radiat Res Appl Sci. 2025;18(1):101298.

[30] Jubair S, Ali B, Rafique K, Mahmood Z, Emam W. Numerical simulation of hybrid nanofluid flow with homogeneous and heterogeneous chemical reaction across an inclined permeable cylinder/plate. Energy Explor Exploit. 2024;42(6):2270–88.

[31] Madhukesh JK, Kalleshachar V, Kumar C, Khan U, Nagaraja KV, Sarris IE, et al. A model development for thermal and solutal transport analysis of non-Newtonian nanofluid flow over a Riga surface driven by a waste discharge concentration. Water. 2023;15(16):2879.

[32] Southerland VA, Anenberg SC, Harris M, Apte J, Hystad P, van Donkelaar A, et al. Assessing the distribution of air pollution health risks within cities: a neighborhood-scale analysis leveraging high-resolution data sets in the bay area, California. Environ Health Perspect. 2021;129(3):037006.

[33] Li S, Leng Y, Atta G, Ahmad S, Ali K, Idris SA, et al. Thermal attributes of sodium alginate ($Na.C_6H_7O_6$) based binary and ternary hybrid nanofluids under activation energy and induced magnetic field environment. Case Stud Therm Eng. 2024;59:104449.

[34] Weidman PD, Kubitschek DG, Davis AMJ. The effect of transpiration on self-similar boundary layer flow over moving surfaces. Int J Eng Sci. 2006;44(11–12):730–7.

[35] Merkin JH. On dual solutions occurring in mixed convection in a porous medium. J Eng Mathematics. 1986;20(2):171–9.

[36] Merrill K, Beauchesne M, Previte J, Paullet J, Weidman P. Final steady flow near a stagnation point on a vertical surface in a porous medium. Int J heat mass Transf. 2006;49(23–24):4681–6.

[37] Weidman PD, Sprague MA. Flows induced by a plate moving normal to stagnation-point flow. Acta Mech. 2011;219(3):219–29.

[38] Harris SD, Ingham DB, Pop I. Mixed convection boundary-layer flow near the stagnation point on a vertical surface in a porous medium: Brinkman model with slip. Transp Porous Media. 2009;77:267–85.

[39] Shuaib M, Shah RA, Durrani I, Bilal M. Electrokinetic viscous rotating disk flow of Poisson-Nernst-Planck equation for ion transport. J Mol Liq. 2020;313:113412.

[40] Patil A. A modification and application of parametric continuation method to variety of nonlinear boundary value problems in applied mechanics, Thesis, Rochester Institute of Technology; 2016.

[41] Abolbashari MH, Freidoonimehr N, Nazari F, Rashidi MM. Entropy analysis for an unsteady MHD flow past a stretching permeable surface in nano-fluid. Powder Technol. 2014;267:256–67.

[42] Das S, Chakraborty S, Jana RN, Makinde OD. Entropy analysis of unsteady magneto-nanofluid flow past accelerating stretching sheet with convective boundary condition. Appl Math Mech. 2015;36:1593–610.